Wave-GAN: A deep learning approach for the prediction of nonlinear regular wave loads and run-up on a fixed cylinder

Blanca Pena and Luofeng Huang[1]

Department of Mechanical Engineering, University College London, London, United Kingdom

Abstract

Machine learning techniques have inspired reduced-order solutions in the fluid mechanics' field that benefit from unprecedented capability and efficiency. Targeting ocean-wave problems, this work has developed a novel data-driven computational approach, named Wave-GAN. This new tool is based upon the conditional Generative Adversarial Network (GAN) principle, and it provides the ability to predict three-dimensional nonlinear wave loads and run-up on a fixed structure. The paper presents the principle of Wave-GAN and an application example of regular waves interacting with a vertical fixed cylinder. Computational Fluid Dynamics (CFD) is used to provide training and testing datasets for the Wave-GAN deep learning network. Upon verification, Wave-GAN proved the ability to provide accurate results for predicting wave load and run-up for wave conditions that were not informed during training. Yet the CFD-comparative results were only obtained within seconds by the deep learning tool. The promising results demonstrate Wave-GAN's outstanding potential to act as a pioneering sample of applying machine learning techniques to ocean-wave interaction problems. It is envisioned that the new approach could be extended to more complex shapes and wave conditions to facilitate the early design stage of marine and offshore engineering applications such as monopiles. As a result, enhanced reliability is expected to prevent environmental disasters in the offshore industry.

Keywords: Machine Learning, Deep Learning, Generative Adversarial Network, Image processing, Ocean waves, Wave load, Monopile.

[1]corresponding author: ucemlhu@ucl.ac.uk

1. Introduction

The interactions between ocean surface waves and structures have significant importance in various environmental and engineering problems, such as the safety and durability of coastal/offshore structures (Liu et al., 2009; Pavlou and Li, 2018), the performance of ships and floating facilities (Cleary and Rudman, 2009; Rrake et al., 2015; Rajendran et al., 2016; Jiao et al., 2019; Huang et al., 2020), the efficiency of wave energy converters (Anderlini, 2018; Benites-Munoz et al., 2020; Windt et al., 2020), and the natural evolution of waves with sea floors, vegetation and sea ice (Li et al., 2018; Huang et al., 2019; Jacobsen et al., 2019; Li et al., 2020). Therefore, vast scientific and financial resources are being spent studying these processes, including performing physical tests and developing prediction models. Experimental and full-scale tests are the most reliable methods for such purposes; they generate prohibitive cost and are inconvenient to consider fickle wave conditions fully. Therefore, prediction methods have been more generally used in relevant design circles, and their applicabilities are dictated by a compromise between accuracy and computing speed.

Studies on wave-structural interactions (WSI) started with analytical solutions. Generally, the wave fields may be obtained using the potential flow theory. Heins (1950) used the Wiener-Hopf method to predict the reflection and transmission of waves against a plate fixed under the water surface. Morison *et al.* (1950) devised an approximate formula for calculating the unbroken wave loads on fixed vertical cylinders. This method is widely used in the industry but it presents limitations. For example, the Morison equation assumes that the flow acceleration is more-or-less uniform at the body's location, and it requires the diameter of the cylinder to be much smaller than the wavelength. The equation also presents challenges when modelling wave breaking phenomena. Keller and Karal (1960) formulated a geometric theory for wave diffraction against a bottom-mounted vertical cylinder. Subsequently, the diffracted wave solutions were combined with wave-induced structural loads by integrating the fluid force over the structural surface. Rainey (1989) introduced an improved Morrison's equation to predict the wave load on an offshore structure. Faltinsen *et al.* (1995) combined nonlinear velocity attributes in the potential flow theory with the wave load on a fixed vertical cylinder. They demonstrated that the nonlinear effects could give a non-negligible contribution to the wave load.

The analytical solutions mentioned above were only applicable to solving linear or weakly nonlinear WSI due to their formulation's inherent linearity (Pena and McDougall, 2016). In real life, relevant engineering design usually needs to consider significant nonlinearities, since it is of more interest to consider rough wave conditions, i.e. the conditions that easily expose structural issues. For this reason, instead of analytical solutions limited to mild WSI, the contemporary development of WSI prediction methods has focussed on the computational fluid dynamics (CFD) technique. CFD numerically solve the nonlinear Navier–Stokes equations, by which it is possible to obtain a fully matched solution between the wave field and the structure. Following validation against experiments, the accuracy of CFD in predicting WSI has been widely proved. For example, Buldakov *et al.* (2019) reported parallel CFD and experimental presentations of the evolution of highly nonlinear focussed wave groups. Liu *et al.* (2019) compared CFD and experimental results of the load from violent breaking waves on a vertical wall; Lyu *et al.* (2019), Chen *et al.* (2019) and Brown *et al.* (2020) accurately predicted the load of focussed wave groups on a fixed or floating cylinder.

Nonetheless, a CFD simulation requires a relatively long time to complete, and CFD may not always be accurate because the solution is highly dependent on the user's setup. Usually, large-scale verifications and validation are required before a CFD model can be acceptable, which means CFD cannot be directly compatible with applications requiring rapid computing. In early design stages, it would be of great help to have an alternative method that is very fast and can provide comparative prediction as CFD does. This approach may sound self-contradictory in conventional computations, as high precision is based upon computational complexity - in most cases, the solution accuracy increases with the computational time.

In recent years, data-driven solutions, known as Machine Learning (ML), have provided the possibility to skip the complexities of physical modelling while allowing to obtain accurate and fast solutions. These models are highly flexible and can be generalised to 'unseen' data not used to build and calibrate the Machine Learning algorithm. Data-driven techniques have shown a vast potential of application in various engineering fields such as wind energy (Bre et al., 2018), aerospace engineering (Krishnakumar, 2003) and civil engineering (Reich, 1997). Also, a series of examples of ML applications in the maritime field has already been demonstrated from ship design, marine engineering and ship operation optimisations (Pena et al., 2020). However, the application of ML in offshore engineering where strong wave-structure interactions exist is still understudied.

Depending on how the learning task is achieved, data-driven algorithms can be classified into two broad categories: Supervised Learning and Unsupervised Learning. Supervised learning algorithms rely on a set of input dataset whose characteristics, output and relationship are known and the data used to train the algorithm is labelled. By contrast, unsupervised learning finds structures in non-labelled data with no human supervision needed during the training. The majority of current models are based on shallow Artificial Neural

Network (ANNs) configurations inspired by the biological brain. They are made by multiple artificial neurons which receive a signal, then processes it and sends it to neurons connected to it. A signal, which is represented by a number, is computed by a certain nonlinear function that is assigned a weight with its value been adjusted as the learning takes place. Neurons are typically grouped into layers and the signal travels from the input layer to the output layer (a signal can pass layers multiple times). While shallow ANNs require a relatively small amount of data, they lack generalisation for the data far away from the training data. For this reason, large numbers of data are usually needed in the training process to enhance the model generalisation for complex problems. By contrast, deep learning approaches, as illustrated in Fig. 1, provide a possibility to handle this problem. The successful applications in the area of computer vision (O'Mahony et al., 2019) and Natural Language Processing (Young et al., 2018) have recently drawn researchers' attention to deep learning methods in the field of structural mechanics and fluid mechanics (Young et al., 2018). More recent examples of Deep Learning applications can be found in (Rabault et al., 2020; Viquerat et al., 2021).

Deep Learning regressors have provided average characteristics of the flow in aerodynamics, accounting for nonlinearities of the flow. However, conventional deep learning is still lacking the possibility to provide more detailed information such as the flow unsteadiness. Generative adversarial networks (GANs) are an approach to generative modelling using deep learning methods, such as convolutional neural networks., It can remedy the limitation of conventional deep learning by generating various types of data and innovated in theory and model structure, thus investigating nonlinear phenomena and unsteady flow fields (Lee and You, 2019). GANs offer the possibility to model the whole flow fields in the form of images.

In such a context, this work aims to build ML deep learning models for predicting mean and fluctuating wave pressures around smooth circular cylinder fixed to the seabed under various wave conditions. The new tool, named Wave-GAN, successfully bridges the gap of yielding a rapid and reliable solution for WSI; in public space, Wave-GAN should be the first one achieving this purpose. In the present work, deep learning GANs are preferred among other regression supervised learning approaches due to their ability to predict highly nonlinear phenomena such as the evolution of steep waves on a structure and other unsteady phenomena inherent in the flow that regression methods might miss. Wave-GAN is trained based on CFD datasets to predict the hydrodynamic interaction of regular waves with a vertical fixed cylinder. Following this introduction, Section 2 gives an overview of the methodology followed to build the Wave-GAN, including the CFD model used to obtain the datasets, a brief introduction to the data-driven predictive method, data mining, and the quantitative index to evaluate the accuracy of Wave-GAN. Subsequently, Section 3 gives a detailed explanation of the Wave-GAN principles and architecture. In Section 4, the results obtained by the Wave-GAN for wave conditions that were not informed during training are compared with the ones calculated by CFD, and the accuracy is analysed in detail to verify the novel Wave-GAN deep learning method. Section 5 discusses the usage and benefits of such a deep learning tool in realistic engineering applications. Section 6 summarises this work with its implications. Overall, the readers can expect to study a heuristic approach for applying deep learning techniques in WSI problems.

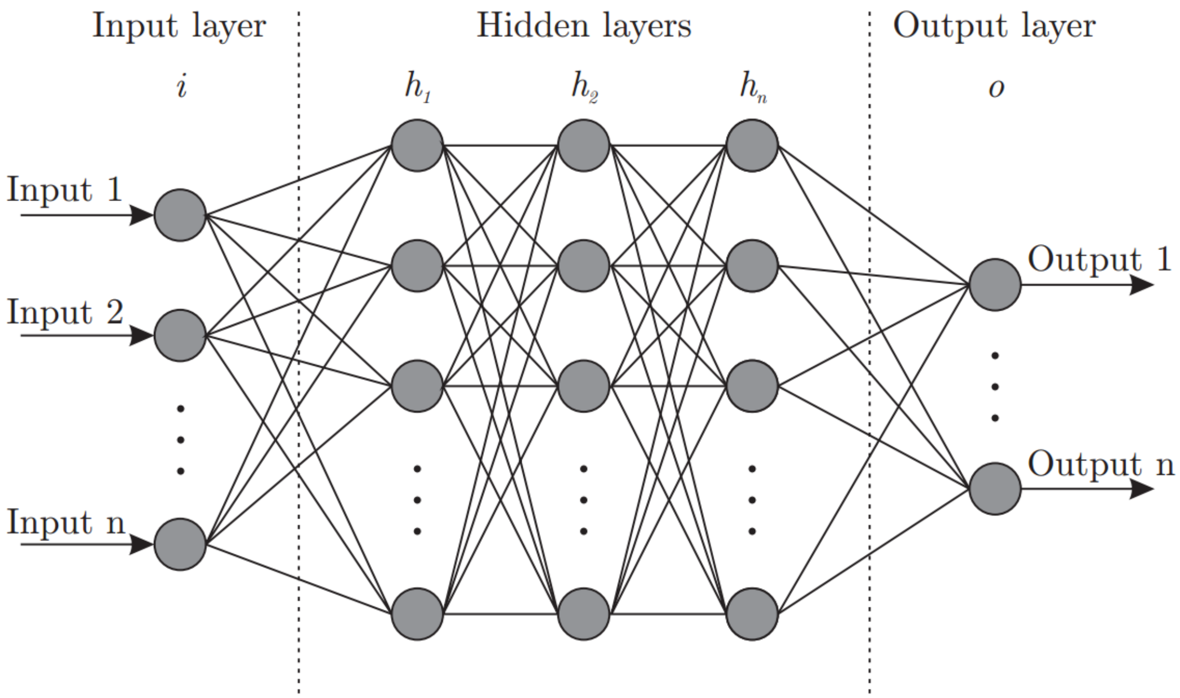

Fig 1: A flowchart of deep learning approaches (Bre et al., 2018); by contrast, a shallow learning approach would only have one hidden layer.

2. Methodology

2.1 CFD Method

Three-dimensional fully nonlinear numerical simulations of regular waves propagating against a fixed vertical cylinder were conducted using the STAR-CCM+ CFD code. The solution of the fluid domain was obtained by solving the Reynolds-Averaged Navier-Stokes (RANS) equations for an incompressible flow:

$$\nabla \cdot \overline{\boldsymbol{v}} = \mathbf{0} \tag{1}$$

$$\frac{\partial\, (\rho \overline{\boldsymbol{v}})}{\partial t} + \nabla \cdot (\rho \overline{\boldsymbol{v}\boldsymbol{v}}) = -\nabla \overline{\mathrm{p}} + \nabla \cdot (\overline{\tau} - \rho\, \overline{\boldsymbol{v}'\boldsymbol{v}'}) + \rho \mathrm{g} \tag{2}$$

where $\overline{\mathbf{v}}$ is the time-averaged velocity vector and $\mathbf{v}'$ is the fluctuating component, ρ is the fluid density, $\overline{p}$ denotes the time-averaged pressure, $\overline{\tau} = \mu[\nabla \mathrm{v} + (\nabla \mathrm{v})^{\mathrm{T}}]$ is the viscous stress term, μ is the dynamic viscosity and g is gravitational acceleration set at 9.81 m/s^2. The k−ω SST model (Menter, 1993) was implemented along with the Reynolds-Averaged Navier Stokes (RANS) equation to model the turbulence.

The free surface between the air and water was modelled by the Volume of Fluid (VOF) method (Nichols and Hirt, 1979). The VOF method introduces a passive scalar α, denoting the fractional volume of a cell occupied by a specific phase. In this case, a value of α = 1 corresponds to a cell full of water and a value of α = 0 indicates a cell full of air. Thus, the free surface, which is a mix of these two phases, is formed by the cells with $0 < \alpha < 1$. The elevation of the free surface along time is obtained by the advection equation of α, expressed as Equation (3). For a cell containing both air and water, its density and viscosity are determined by a linear average according to Equation (4) and Equation (5).

$$\frac{\partial \alpha}{\partial t} + \nabla \cdot (\overline{\mathbf{v}} \alpha) = 0 \tag{3}$$

$$\rho = \alpha \rho_{water} + (1 - \alpha) \rho_{air} \tag{4}$$

$$\mu = \alpha \mu_{water} + (1 - \alpha) \mu_{air} \tag{5}$$

In this study, ρ_{water} = 1000 kg/m^3, μ_{water} = 8.90×10^{-4} N·s/m^2; ρ_{air} = 1 kg/m^3, μ_{air} = 1.48×10^{-5} N·s/m^2.

The governing equations were applied to a discretised cuboid tank as shown in Fig. with the x-axis being parallel to the wave advancing direction and the z-axis is positive upwards. A cylinder of 0.05 m diameter (L) is vertically installed in the domain, at the midplane along the y-axis. The domain was filled with water to a depth of 2 m, with air filling the remainder. At the top boundary of the domain, a static pressure boundary condition was applied to represent atmospheric conditions whereas the bottom boundary was defined as a no-slip wall to account for the seabed presence. The two side planes were defined as symmetry planes. A Dirichlet condition was applied at the inlet and pressure at the outlet.

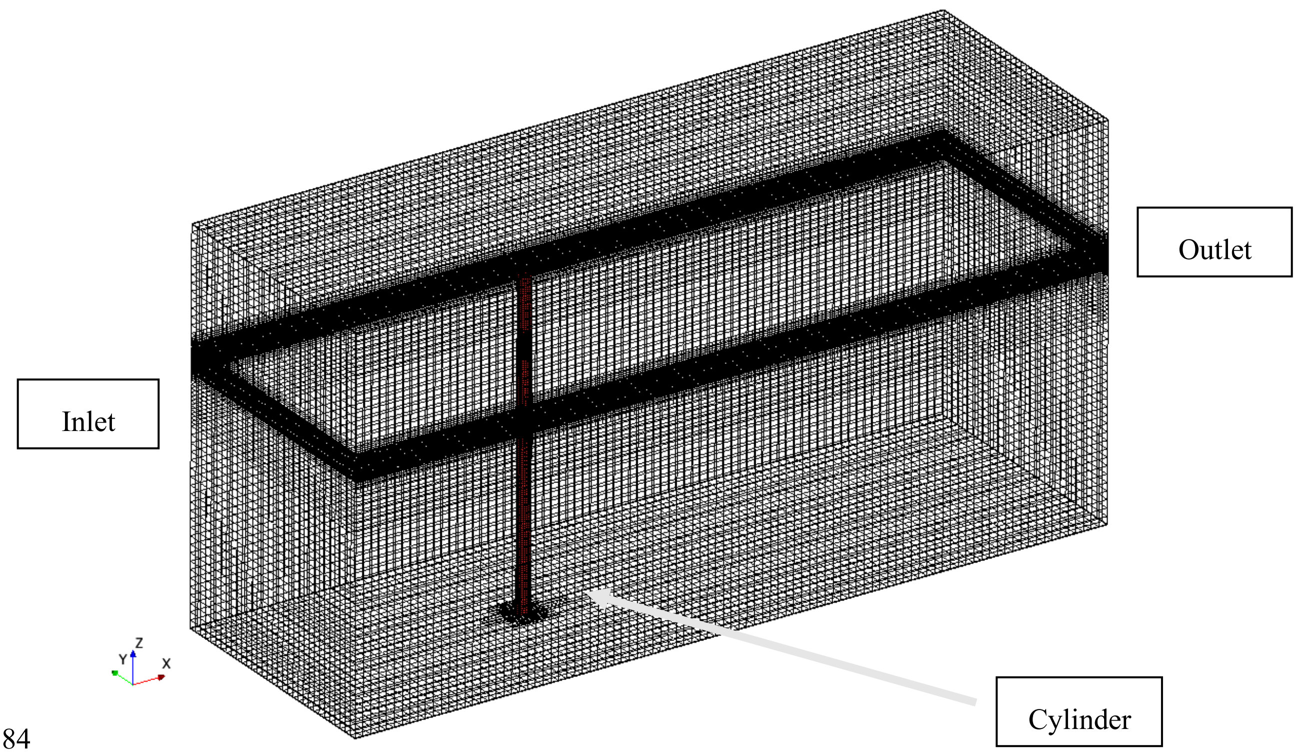

Fig. 2: Computational domain for obtaining the RANS solution.

Periodic regular waves were generated at the inlet boundary, propagating in the positive *x*-direction, and a wave absorption zone was placed at the outlet to eliminate the reflection of waves from the outlet boundary. The wave generation and absorption were realised following the fifth-order Stokes theory for nonlinear waves (Dean and Dalrymple, 1984). Equation (6) – (8) give the solutions of the first two orders, since the full equations are lengthy. Fifth order Stokes waves were selected since the Ursell number (U) was not exceeding 46.7. The Ursell number indicates the nonlinearity of long surface gravity waves and is defined as $U = H\lambda^2 / h^3$, where H represents the wave height, h the mean water depth, and λ is the wavelength. This approximation is acceptable in shallow waters and it has been validated with experiments in the literature (Zhao et al., 2016).

$$\eta = D + \frac{H}{2}\cos(kx - \omega t) + \frac{H^2 k}{16}\frac{\cosh(kh)}{\sinh^3(kh)} \times [2\cosh(2kh)] \times \cos 2(kx - \omega t) \tag{6}$$

$$v_x = \frac{Hgk}{2\omega}\frac{\cosh(ky+kh)}{\cosh\,(kh)}\cos(kx - \omega t) + \frac{3}{16}\frac{H^2\omega k \times \cosh\,2(kh+ky)}{\sinh^4(kh)} \times \cos 2(kx - \omega t) \tag{7}$$

$$v_y = \frac{Hgk}{2\omega}\frac{\sin(ky+kh)}{\cosh\,(kh)}\sin(kx - \omega t) + \frac{3}{16}\frac{H^2\omega k \times \sinh\,2(kh+ky)}{\sinh^4(kh)} \times \sin 2(kx - \omega t) \tag{8}$$

in which η is the free surface elevation, v_x and v_y are horizontal and vertical velocity components, respectively. H is the wave height, k is the wavenumber, and ω is the angular frequency.

Inside the wave absorption zone, waves are dissipated by an artificial damping force to achieve a still water surface. Specifically, in the wave absorption zone, the momentum Equation (2) is modified into:

$$\frac{\partial(\rho\bar{v})}{\partial t} + \nabla\cdot(\rho\overline{\boldsymbol{v}\boldsymbol{v}}) = -\nabla\bar{\mathrm{p}} + \nabla\cdot(\bar{\tau} - \rho\,\overline{\boldsymbol{v}'\boldsymbol{v}'}) + +\rho\mathrm{g} + \rho\varphi(\boldsymbol{v} - \boldsymbol{v}_{\boldsymbol{str}}) \qquad (9)$$

The last term is the artificial damping force that dissipates the wave motion, where φ is the damping coefficient in units of s^{-1}, and it increases smoothly in the wave propagation direction. $\boldsymbol{v}_{\boldsymbol{str}}$ is the background stream velocity that is exempted from damping, which equals zero when there is no current.

The computational domain sizes are 120 L and 40 L in the streamwise and the spanwise directions, respectively, where L is the cylinder diameter. The cylinder was placed at a distance of 40 L from the inlet. The length of the wave absorption zone is 38 L, where 38 L equals approximately twice the maximal incident wavelength examined in this study. The above dimensions were determined by sensitivity tests to ensure the boundary effects are in line with the physical conditions.

Using the finite volume method, a hexahedral unstructured mesh type was used to discretise the fluid domain with local refinements at the cylinder proximity where a higher resolution of the flow was required. A second-order spatial resolution scheme was used to solve the RANS equations. Mesh sensitivity tests were performed on three mesh sizes G.1, G.2 and G,3, which is a standard CFD procedure to check the convergence (Pena et al., 2019). The timestep was adjusted to achieve a Courant Number of around 1, a well-established rule of thumb. As shown in Table 1, a convergent solution for the maximum load during a wave period (F_{max}) was achieved with half a million cells, with the variance (ΔF_{max}) between G.2 and G.3 to be a minimal level (0.51%).

The applied CFD approach has been following mature guidelines of the field, e.g. ITTC (2017), which has been extensively validated to be highly accurate, while it should be remarked that the focus of the present study is not about the accuracy of CFD but the capability of using a machine learning approach to obtain comparative outcomes in a fraction of time.

Table 1: Mesh Convergence Study of the CFD model

Mesh	Cell number (Million)	F_{max} (N)	ΔF_{max} (%)
G.1	0.23	1.89	-
G.2	0.50	1.98	4.54
G.3	0.74	1.97	-0.51

2.2 Data-Driven Deep Learning Predictive Model

Nonlinear wave impact loads and wave run-up were predicted using the Wave-GAN that was built as part of this work. The Wave-GAN is based on the conditional Generative Adversarial Networks (cGAN) principle which has been successfully used to solve multiple image-to-image translation problems from maps to satellite images (Isola et al., 2017). Input and output datasets were the essential elements to train and test the performance of Wave-GAN, and they were obtained from the CFD computations described in the previous section. More details of the Wave-GAN architecture and training will be presented in the forthcoming sections.

2.3 Data Mining

A series of CFD simulations were created to account for different wave profile scenarios. Wavelengths ranging from 0.5 m to 1.5 m in intervals of 0.1 m together with wave heights between 0.05 m to 0.1 m in intervals of 0.01 m were defined at the inlet corresponding to Keulegan–Carpenter (KC) numbers ranging from 2.5 to 5 and 5 different wave amplitudes. The KC number is defined as $KC = a_x T/L$, where a_x is the surge amplitude of wave oscillation, T is the wave period and L is the characteristic length of the structure. A small KC value indicates that the drag force that comes from the viscosity is negligible compared to inertial forces, whilst a high KC means considerable turbulent behaviours.

After the convergence of each simulation, screenshot datasets composed of input and output images were recorded every 0.002 s and ensuring that at least one full wave period was documented for each simulation case. In total, 55 simulations with different wave amplitude and length were conducted, and approximately 100,000 screenshots of input and output images were extracted.

On the one hand, input images represent the superimposition of an undisturbed wave field and a cylinder with a diameter L as shown in Fig. . While input images can be sketched manually using Paint, Photoshop, MATLAB and Excel, this study extracted them directly from the CFD software.

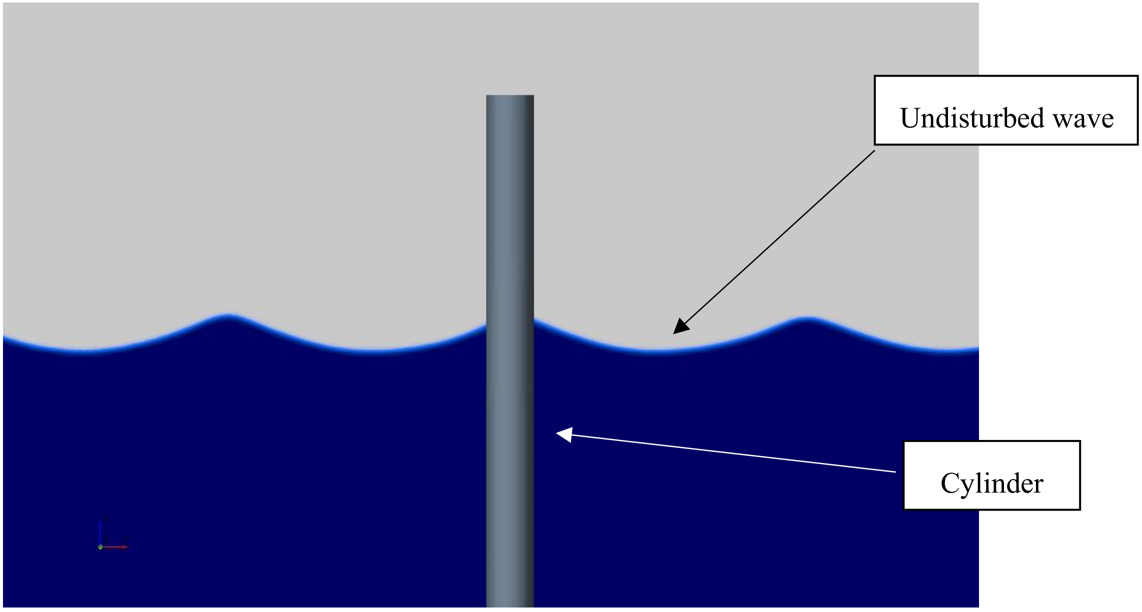

Fig. 3: Sample of an input image.

On the other hand, output images represent the 'disturbed' wave field together with the wave load on the cylinder's surface, as shown in Fig. 4. During the present work, dynamic pressure was chosen as the predicted target of the network algorithm, considering its relevance to the design of offshore structures such as monopiles, rigs and ships. The scale of dynamic pressure used during the present study is as included in Fig. 4, which ranges from -500 Pa to 1000 Pa; this could be also replaced by pressure coefficient. And yet, following the same approach, the Wave-GAN could be trained to predict other parameters such as flow velocities or more complex fluid-structure interaction parameters.

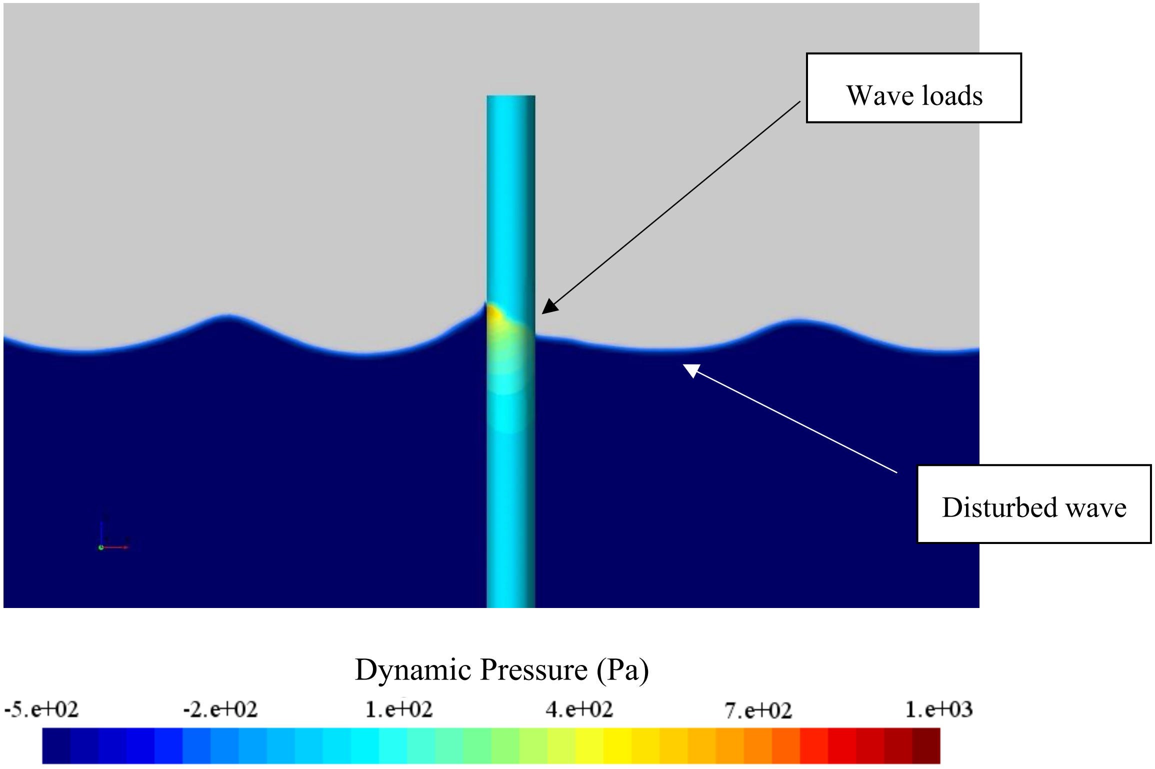

Fig. 4: Sample of an output image. The contour for dynamic pressure is consistent with all the following pictures.

Once all the datasets were generated, they were separated into two distinct groups: training and testing – out of the generated pictures, 20% of the data was used for training, 40% for dev and the remaining 40% was employed for testing purposes. Each dataset contains an input picture serving as ground truth and an output picture used to judge Wave-GAN's accuracy.

2.4 Error Quantification

As part of this study, the error between predicted and ground truth images (CFD calculation) was estimated by using the Mean Absolute Error (MAE) technique. The MAE is described in Equation (10), where y_i represents the ith pixel intensity for the predicted image, $\hat{y}_i$ is the ith pixel intensity for the ground truth and m is the number of pixels.

$$MAE = \frac{1}{m}\sum_{i=1}^{m}[(y_i - \hat{y}_i] \qquad (10)$$

3. Generative Adversarial Network

3.1 Overall Wave-GAN Principle

The algorithm was conceived as a supervised learning generative model suitable for building one-to-one mapping from a given condition into predictions of wave loads and run-up on a cylinder. The Wave-GAN, which is based on GAN's principle (Goodfellow et al., 2014), was therefore formulated as a minimax two-player game between two distinct deep learning network models - (a) a Generator 'G' which is responsible to create samples that are intended to come from the same distribution as that of the real data and, (b) a discriminator 'D' that determines whether the sample from the target domain is a real (ground truth) or a generated version of the source image. This process is illustrated in Fig. 5.

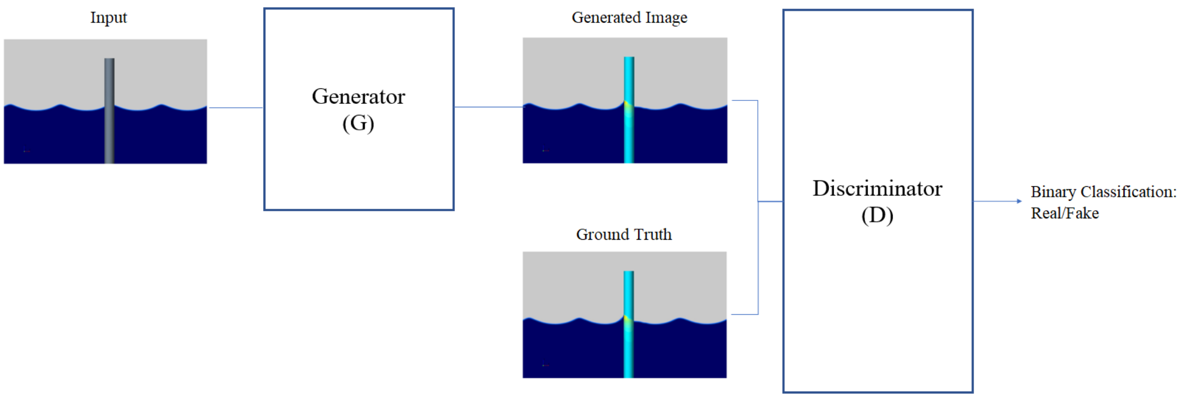

Fig. 5: Overall Wave-GAN training principle for wave load prediction and run-up on a cylinder.

3.2 Loss Functions

As reported in the literature, the objective of a cGAN can be expressed as (Isola et al., 2017):

$$\mathcal{L}_{cGan}\,(G,D) \;=\; \mathbb{E}_{x.y}[log\;D\;(x,y)] + \mathbb{E}_{x.z}[log(1-D(x,z))] \tag{11}$$

where G, the generator, tries to minimise this objective against an adversarial discriminator, D. The Generator G is optimised by playing a min-max game with the Discriminator D in the form of:

$$G^* = arg\ min_G max_D\ \mathcal{L}_{cGan}\ (G, D) \tag{12}$$

Previous studies reported that it is beneficial to mix the GAN objective with a more traditional loss, such as L1 distance which encourages less blurring (Isola et al., 2017) and which is defined as follows:

$$\mathcal{L}_{L1}\ (G)\ =\ \mathbb{E}_{x.y}[\|y - G\ (x, z)\|_1] \tag{13}$$

Therefore, the final objective of Wave-GAN considering L1 distance is:

$$G^* = arg\ min_G max_D\ \mathcal{L}_{cGan}\ (G, D)\ +\ \lambda\,\mathcal{L}_{L1}\ (G) \tag{14}$$

3.3 Network Architecture

The Wave-GAN generator architecture, as shown in Fig. 6, follows an encoder-decoder structure with skip connections between mirrored layers in the encoder and decoder stacks, also called a modified U-net (Olaf Ronneberger et al., 2015). Note that skip connections were established between *i* and *n-i* layers where n is the total number of layers.

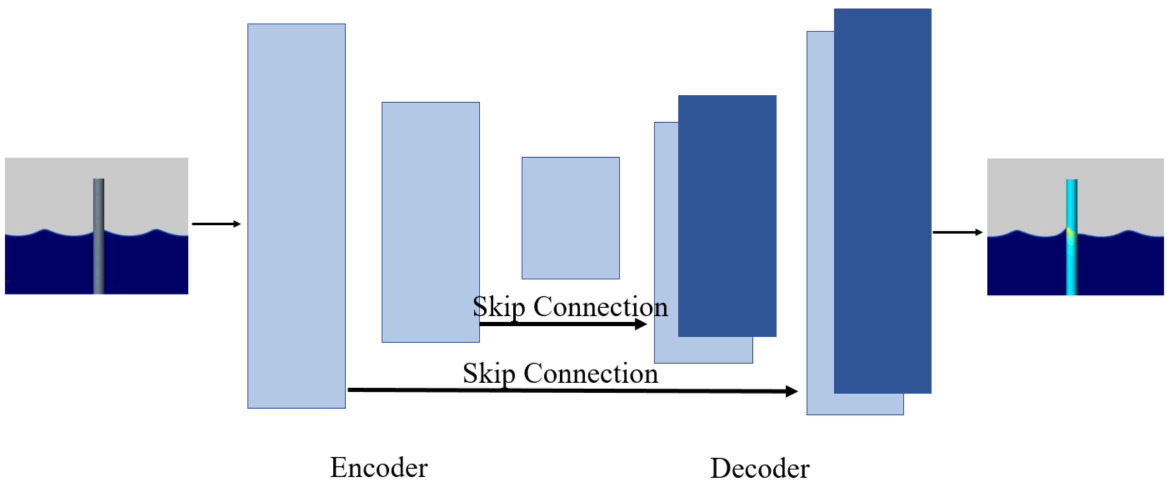

Fig. 6: Generator fundamental structure following a U-Net with skip connections.

The generator uses modules of the form convolution-BatchNorm-ReLu (Leaky ReLU) (Ioffe and Szegedy, 2015) as described in (Isola et al., 2017). The encoder structure obeys the structure c64-c128-c256-c512-c512-c512-c512-c512-c512 as shown in Fig. 7, where *ck* denote a Convolution-BatchNorm-ReLU layer with *k* filters. All convolutions are run with a 4x4 kernel size, a stride of 2 and the convolution in the encoder was programmed to downsample by a factor of 2. Batch-Norm is not applied to the first c64 layer in the encoder. In the decoder part, however, the upsampling process is done from the latent high dimensional vector back to the original input size sequentially. The decoder follows a cd512-cd512-cd512-c512-c512-c256-c128-c64 architecture as shown in Fig. 7, where *cdk* denotes a Convolution-BatchNorm-Dropout-ReLU layer with *k* filters and with a dropout rate of 50%. Note that convolutions upsamples by a factor of 2. In the decoder, after the last layer, a convolution is applied to map to the number of outputs 3 RGB channels followed by a tanh activation function. All ReLUs in the encoder are leaky, with a slope of 0.2, while ReLUs in the decoder are not leaky. The architecture presented was found by conducting a careful meta-parameter study.

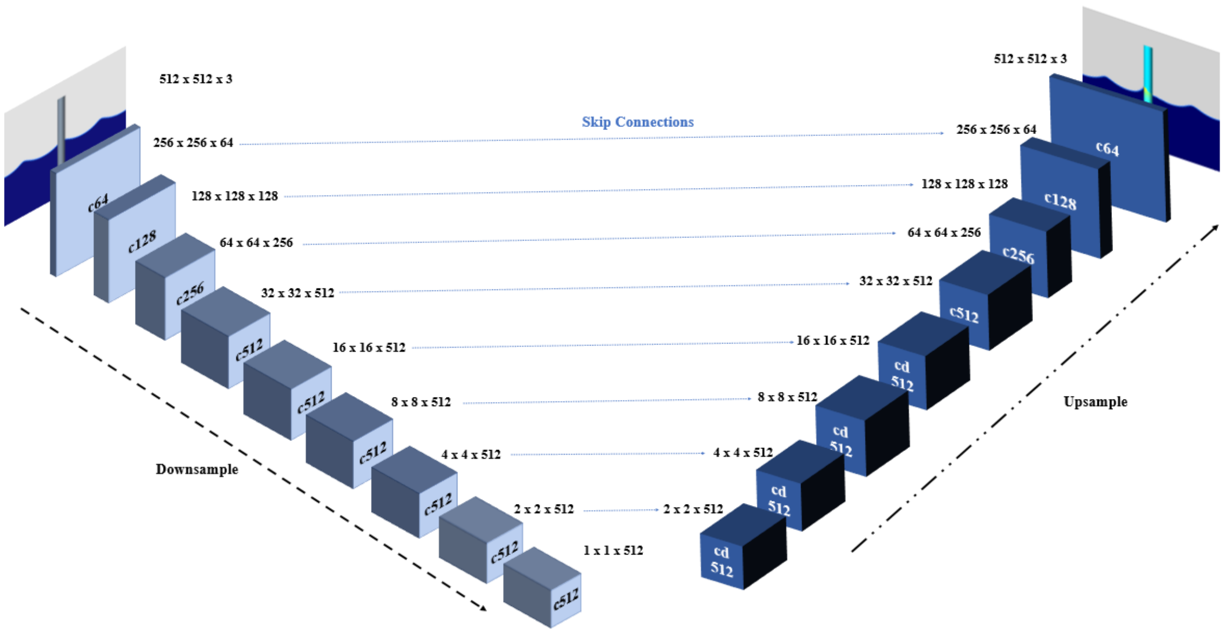

Fig. 7: Architecture of the generator.

The discriminator follows a PatchGAN structure (Li and Wand, 2016) where 70x70 patches aim to classify if a generated image is real or fake. The discriminator was also defined by modules of the form convolution-BatchNorm-ReLu (Leaky ReLU) (Ioffe and Szegedy, 2015) and its architecture follows a c64-c128-c256-c512 structure with a kernel size of 4x4. After the last layer, a convolution is applied with a stride of 1, followed by a Sigmoid activation function. For the discriminator, all ReLUs are leaky, with a slope of 0.2.

With regard to the network performance, this study followed the approach described by Goodfellow *et al.* (2014) by first alternating between one gradient descent step on D and then one step on G. The Wave-GAN was therefore trained to maximise log D (x; G(x; z) as suggested by Goodfellow *et al.* (2014). Besides, the rate at which D learns relative to G was slowed down but dividing the objective by 2. This practice is a recommended practice that has shown to offer stability to the training of GANs (Goodfellow et al., 2014). Minibatch stochastic gradient descent is used and the Adam solver (Kingma and Ba, 2015) is applied with a learning rate of 0.0002, the first moment of 0.5 and the second-moment of 0.99.

4. Results and analyses

4.1 Training

Deep learning models are known to be particularly sensitive to parameters such as the number of training datasets. Therefore, as part of this study, the frequency at which samples were taken for training was studied. This sensitivity test could be particularly beneficial to minimise training times during offshore/marine structures' design, without reducing the results' accuracy.

Three deep learning networks with distinct training datasets were created: Case A, Case B and Case C. All models were trained from scratch, and the weights were initialised from a Gaussian distribution with a mean value of 0 and a standard deviation of 0.02. Case A employs a high period between data samples, whereas Cases B and C use a smaller period between datasets. A summary of the three cases is summarised in Table 2. It can be seen that after an initial training time, Wave-GAN can just take seconds to provide a prediction for a new test condition.

Table 2: Cases used for training with different data sizes.

Case	Frequency	Training Pairs	Training time	Prediction time
A	1/40	2,500	3 hours	
B	1/20	5,000	12 hours	≈ 10 seconds
C	1/10	10,000	1.3 days	

Fig. 8 depicts the ground truth compared with the images generated from the three networks A, B and C at the 300th epoch for datasets not included in the training. Overall, it is possible to see that the number of datasets affects the quality of the generated picture and the prediction of wave loads and run-up on the cylinder. Besides, Case A produces a blurrier load prediction than Cases B and C. This phenomenon is reasonable since the lack of training data is expected to affect the final predictions and the rate at which the networks learn. However, it is essential to note that training a model with more datasets significantly increases the computational power required to train the network. Table 2 displays the necessary time to train each of the models using a Tesla V100 GPU and TensorFlow 2.3.1. This result confirms that the training time and computational demand should be considered before running data-driven analyses using GANs.

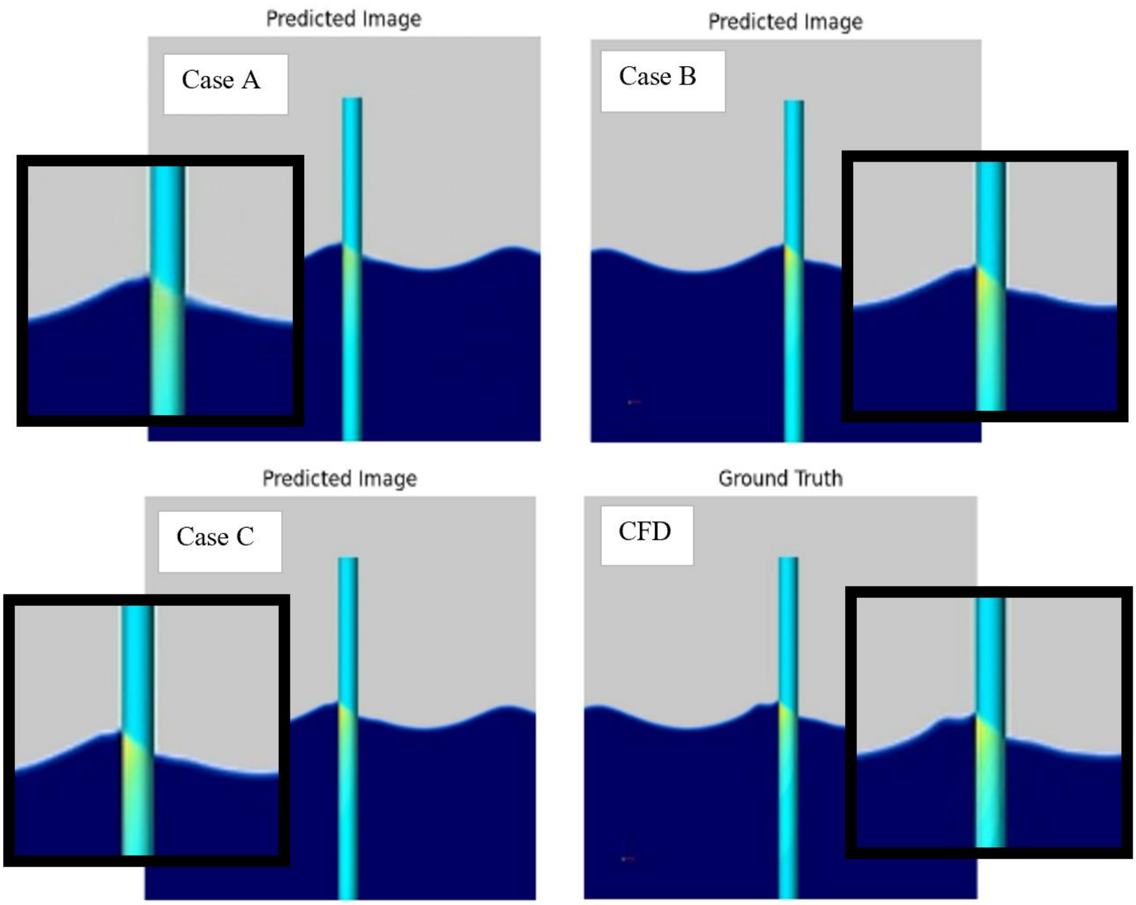

Fig. 8: Wave load predictions for Cases A, B and C vs ground truth (CFD).

Additionally, the prediction accuracy for each model for datasets not included during training was evaluated using MAE, which helped gain further insight into each model's performance. By plotting the MAE in a Box-and-Whisker style chart, it is possible to see if high bias or high variance problems exist and therefore detect overfitting or underfitting issues. Fig. 9 depicts the average MAE values for each of the three cases studied and showing a significant accuracy difference between them. Whilst MAE in Case A is much higher than the others, there is no significant difference between Case B and Case C. This indicates that Case B achieved great generalisation compared to the models with more training datasets while requiring significantly less computational time than Case C (Fig. 9). Case B is deemed as the best choice for further studies, as it can provide an equivalent accuracy as Case C but requiring much less training time and computational memory.

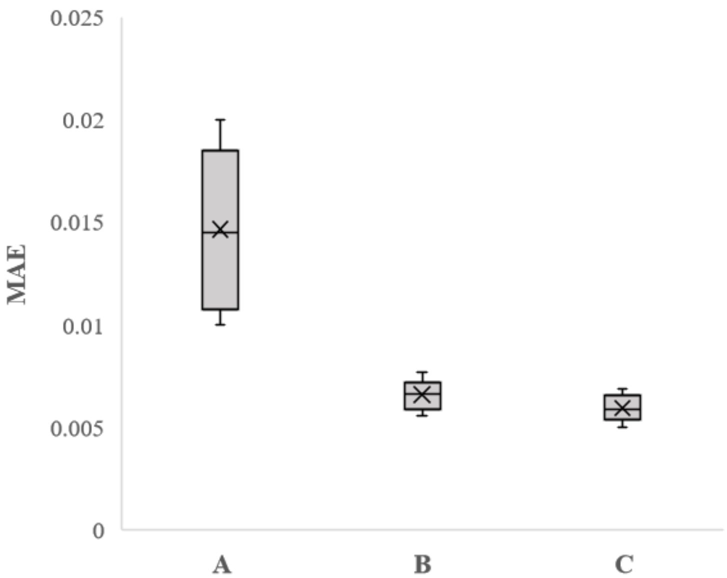

Fig. 9: Average MAE for the three cases.

4.2 Evaluation

Wave-GAN verification is potentially the most crucial step that needs to be carefully assessed to build confidence in the proposed approach. Therefore, a systematic verification using datasets not informed during training was conducted following four steps: (a) convergent study, (b) perceptual observation, (c) localised quantitative comparison, and (d) MAE evaluation.

The first step in validating the Wave-GAN model consisted of examining the overall convergence process and the prediction accuracy during the training phase. Fig. 10 shows the convergence curve, which displays the average generator loss against every epoch. Overall, it can be seen that the process reaches convergence at about epoch 30. In Fig. 11, at epoch 10 the disturbed wave shape was not predicted; At Epoch 30, the generated image is very close to that at Epoch 100, indicating that the Wave-GAN reached a level at Epoch 30 that it cannot learn anymore and the training may be stopped.

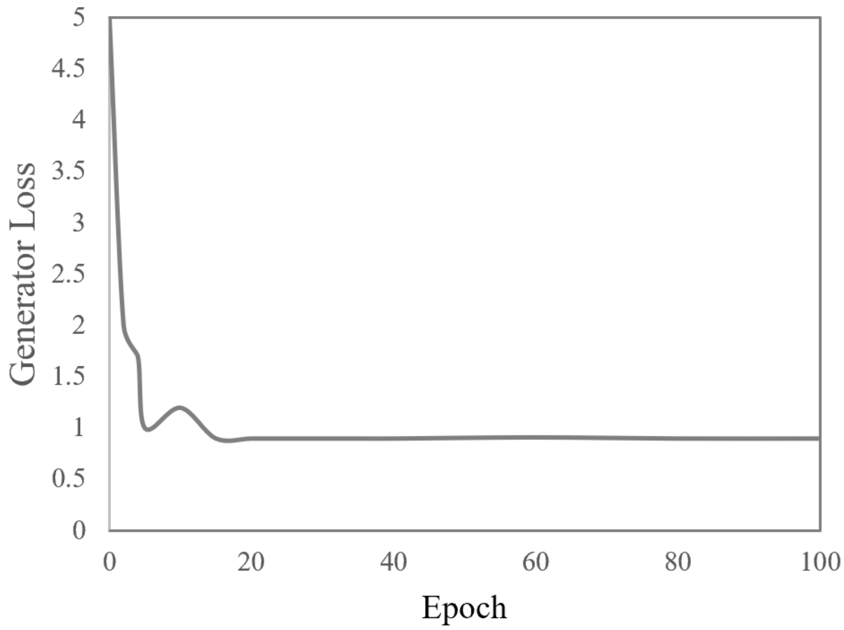

Fig. 10: Convergence of the prediction residual of Wave-GAN.

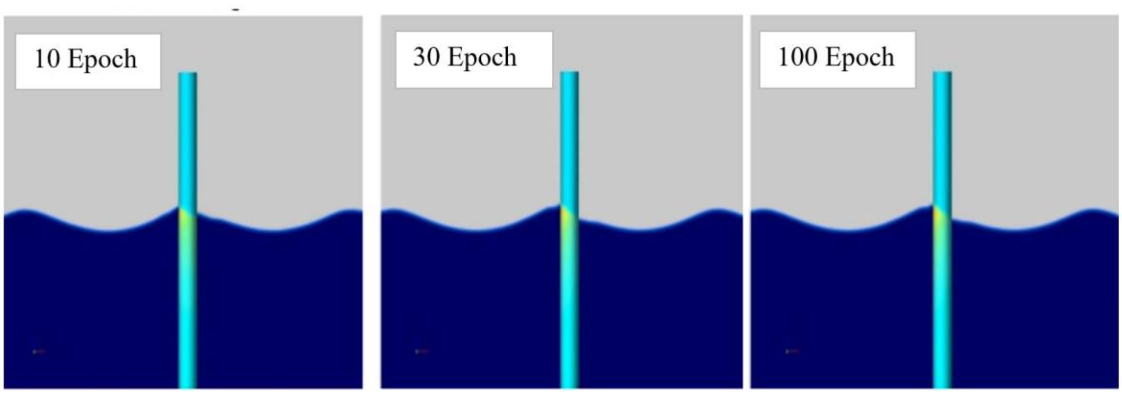

Fig. 11: Wave load and run-up prediction comparison at different epochs.

The second stage of validation was conducted through perceptual comparisons between the predicted images generated by Wave-GAN and the ground truth generated by CFD. Fig. 12-15 depict the hydrodynamic load contours on the cylinder and wave run-up, which correspond to KC numbers between 3.14 and 4.4. Overall, it can be seen that very good agreement between the ground truth and the Wave-GAN prediction was achieved.

In Fig. 12, a KC of 3.14 generated some difference in the disturbed wave pattern prediction, as marked using the red arrows, despite this does not impact the wave run-up prediction. It is interesting to notice that although the disturbed wave pattern is slightly distorted, the wave load still agrees well with CFD. This phenomenon happens because the wave load is predicted using image-processing rather than mathematically from the wavefield.

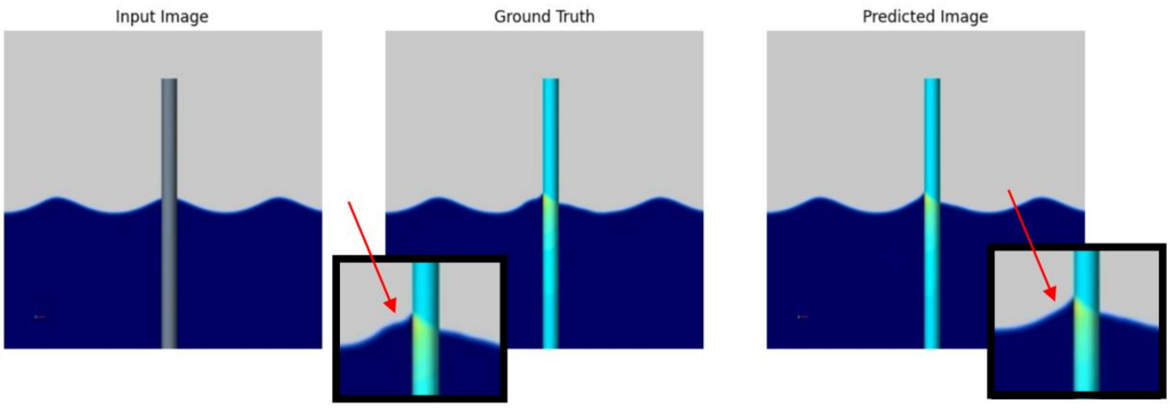

Fig. 12: Input vs ground truth and Wave-GAN prediction at KC = 3.14.

Fig. 13 shows that the disturbed wave pattern has been predicted with a high level of consistency with CFD. The wave load peak (red) has also been predicted by Wave-GAN and demonstrates the image-to-image method for the present application. Besides, Wave-GAN has been able to catch the nonlinearity of the wave pattern, which is becoming sharper as it is approaching the maximum steepness for the given wave.

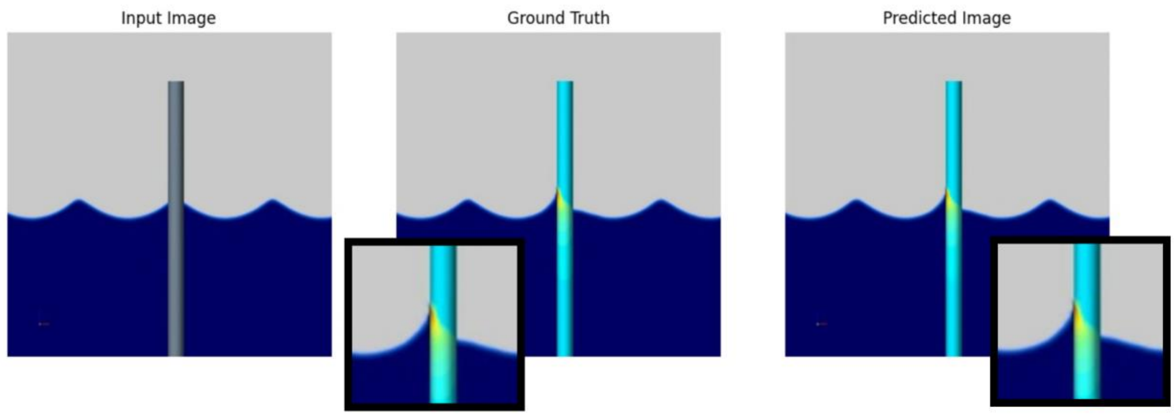

Fig. 13: Input vs ground truth and Wave-GAN prediction at *KC* = 3.54.

A more challenging perceptive test is conducted by passing a very nonlinear and highly steep wave (about to break) by the cylinder, as shown in Fig. 14 and with a *KC* = 4.4. For this challenging condition, the prediction still correlates well with CFD; however, when the pictures are zoomed in (see insert), it can be seen that there is a thin yellow region contouring the peak pressure load (in red) for the ground truth which Wave-GAN has not been able to predict. This phenomenon could happen because the input wave condition is distinctively different from the trained wave conditions. Moreover, when zoomed in, the picture loses resolution, which could potentially affect the predicted loads. This blurriness could be corrected by increasing the input-output layer sizes in the overall structure of Wave-GAN. On the other hand, it can be seen that the disturbed wave has been predicted with a high degree of accuracy regardless of the high nonlinearity of the wave.

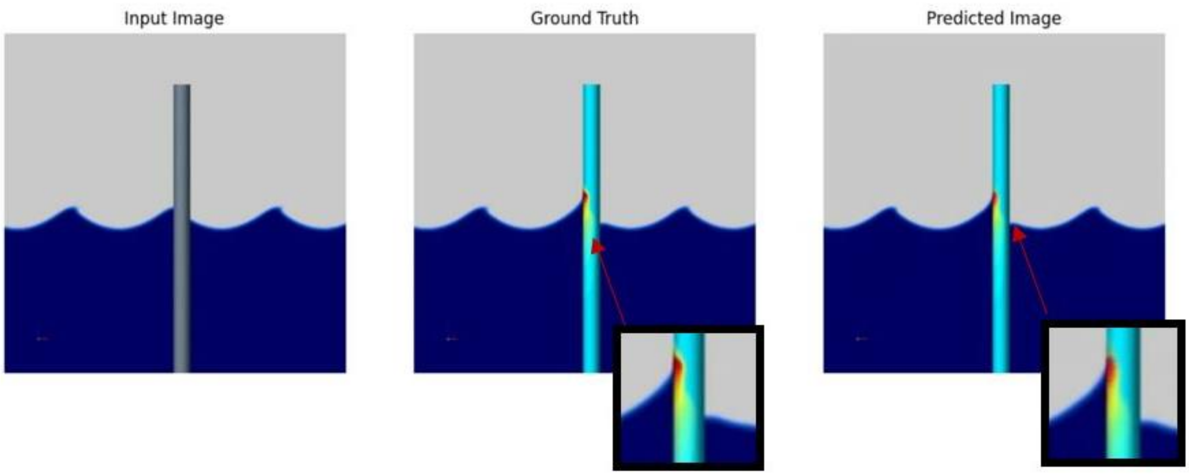

Fig. 14: Input vs ground truth and Wave-GAN prediction at *KC* = 4.4.

It is also of interest to test the wave load and run-up prediction when a trough breaks on the cylinder instead of a peak. Fig. 15, at $KC = 3.14$, depicts that Wave-GAN can accurately predict both wave load and run-up with excellent accuracy regardless of the changed wave phase. Minimal deviances in the contour can be seen as the CFD outputs high-resolution contours for the pressure load. In contrast, Wave-GAN blurs the contour lines by showing a more homogeneous hydrodynamic load on the cylinder. However, the maximum load has been accurately predicted and again confirming the rationality of the present method. Hence, it could be concluded that the position of the wave with respect to the cylinder does not have a notable effect on the accuracy of Wave-GAN in predicting the wave load and run-up.

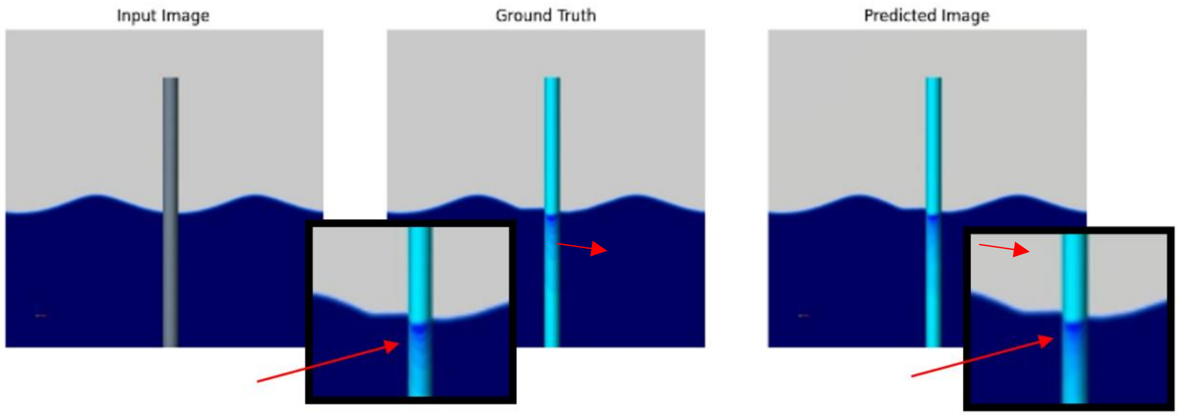

Fig. 15: Input vs ground truth and Wave-GAN prediction at $KC = 3.14$.

Parallel tests on Wave-GAN accuracy with various incident wave heights outside of the training envelope were also performed. Fig. 16 shows a wavelength much longer than the ones contained in the training datasets. It can be seen that the accuracy in the results is fairly high, with minor irregularities in the disturbed wave pattern downstream of the cylinder (indicated by the red arrow). Moreover, the load prediction agrees very well between the ground truth (CFD) and the predicted image. This shows Wave-GAN can be particularly useful to handle vast testing conditions during the early design stage of marine and offshore engineering applications – with a certain number of wave conditions trained, Wave-GAN can provide a reliable prediction for the design containing an extensive range of operation conditions.

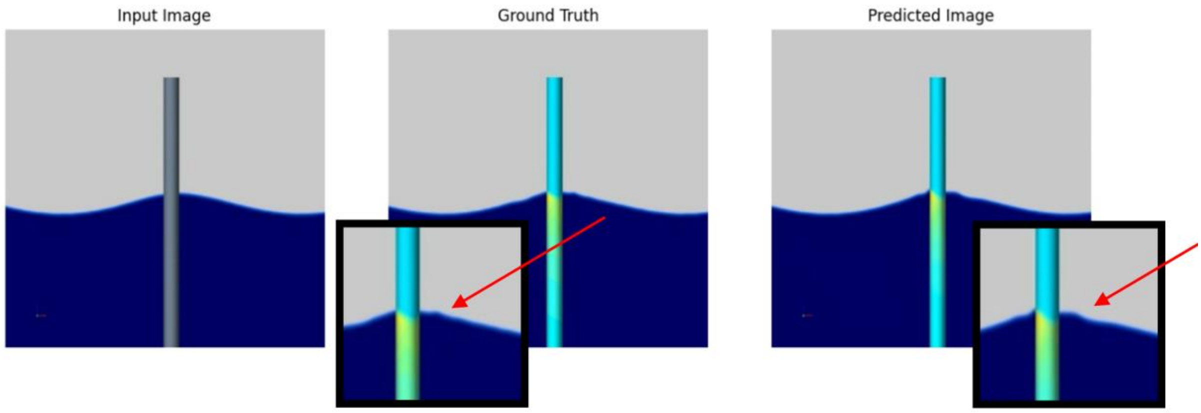

Fig. 16: Input vs ground truth and Wave-GAN prediction at *KC* = 5.0.

A third step in the validation process is conducted by comparing the dynamic pressure distribution over the cylinder diameter at the water depth of 0.5 m and the still free surface, respectively expressed as $z/L = 1$ and $z/L = 0$, as shown in Fig. 17. This plot corresponds to the prediction shown in Fig. 14, which represents a highly nonlinear wave condition. Overall, it is possible to see that pressure for the ground truth and the predicted image correlate well and that the predicted image keeps good accuracy against the CFD results. For $z/L = 1$, a discrepancy of 15% can be observed at $x/L = 0.4$. Although the discrepancy is considerable, it does not impact the accuracy at any of the other locations. At $z/L = 0$, the prediction is very accurate with all deviations being less than 2%. Those discrepancies could be potentially solved with higher-resolution generated images, while the computational cost would increase accordingly if a higher resolution is required.

To provide a direct quantitative metric on how well Wave-GAN can predict the pressure results against CFD, the maximum pressure on the cylinder during a wave period was extracted for all tested cases. Figure 18 displays the average percentage difference between the maximum pressure predicted by CFD and by Wave-GAN, showing that there is a relative difference between 1.6 to 2% for all cases, regardless of the KC number. This comparison depicts that the model is able to predict the maximum load with a high degree of accuracy.

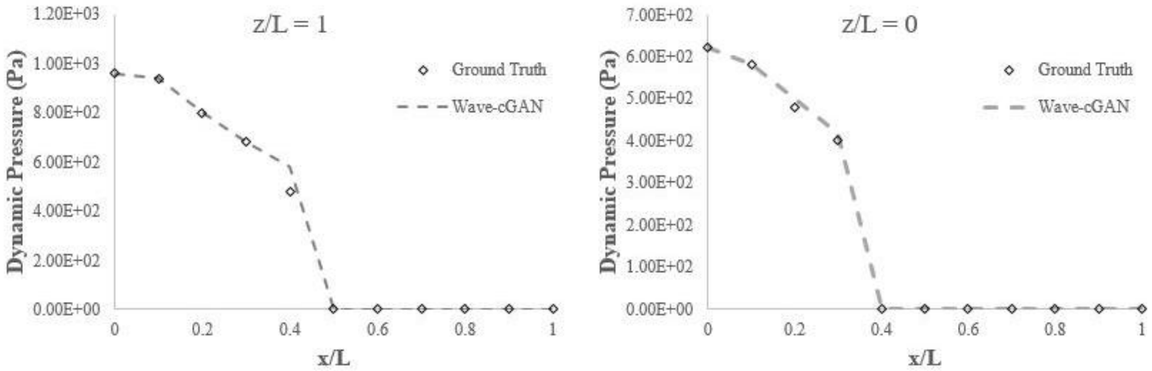

Fig. 17: Dynamic load comparison for ground truth (CFD) and Wave-GAN at two different water depths.

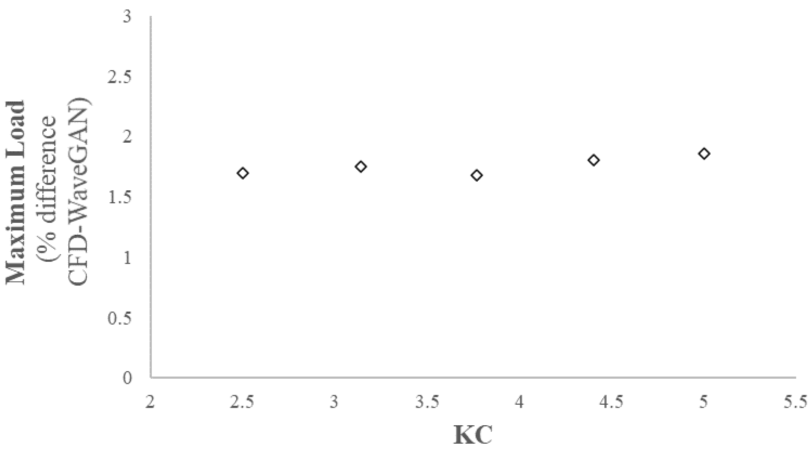

Fig. 18 Relative difference of the maximum pressure on the cylinder, between CFD and Wave-GAN.

Further quantitative validation is conducted by analysing the MAEs for all samples in the training and test sets to ensure that bias and variance are not high. Fig. 19 depicts that the MAE for the training set is smaller than for the testing set. This phenomenon is expected as the training datasets have been passed to Wave-GAN during the training process while the testing dataset has not. Still, the MAEs for the testing dataset are fairly small, even though these correspond to a much more comprehensive wave range than the trained range. Therefore, it can be concluded that Wave-GAN can predict detailed hydrodynamic characteristics rapidly (in less than 10 s as shown in Table 2) and effectively.

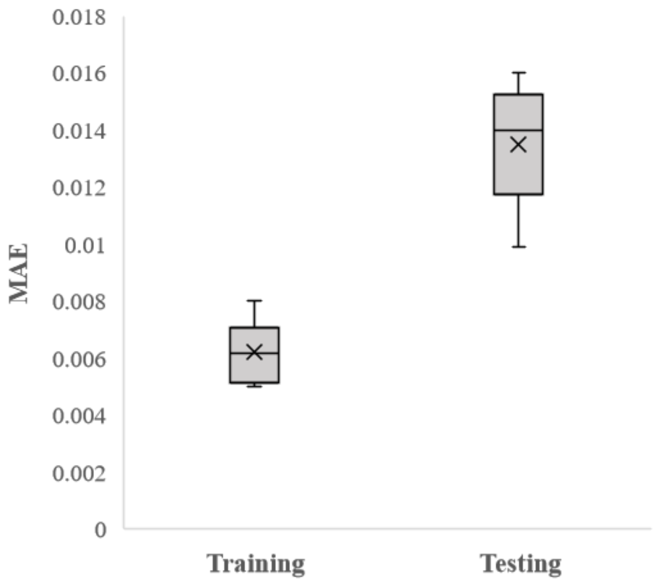

Fig. 19: Average MAE for training and testing datasets.

5. Practicality

It has been demonstrated that Wave-GAN can effectively predict wave-structural interactions as a surrogate approach to CFD. Whilst this is the first demonstration of a deep learning approach for such a purpose, it is of great interest to discuss how such a new tool may be applied in real industrial problems.

(1) Usage

For the academic community, the demonstrated validation of Wave-GAN has shown values to keep developing machine learning models for engineering application; for the industry, since Wave-GAN requires CFD for training, it does not show superior advantages over CFD if it is used on one single design. However, as industrial members (e.g. a classification organisation or a business group) conduct numerous projects per year, provided an initial stage (e.g. hundreds of projects over half to one year period) to extract quality CFD results for training the deep learning model, it is envisioned that Wave-GAN will have the independent ability to provide reliable assessment for the following years, and its capability can still be expanding via additional CFD inputs over time. This means that a wide range of wave conditions, water depths, structural dimensions and structural types will be included, and the model can automatically identify these parameters through the input image.

(2) Benefits

The early design stages will see significant benefits by using Wave-GAN, where vast configurations need to be tested that would be prohibitive to obtain using CFD. Rapid estimates can be provided through Wave-GAN, with nonlinear wave-structural behaviours accounted for, overcoming inaccuracies in contemporarily-used linear analytical methods.

Wave-GAN will provide benefits to the late design stages as its capability and speed allow to evaluate the structural performance for a wide range of wave conditions consisting of infinitely small variations, i.e. a response surface versus different wavelengths and wave heights. Benefited from the improved accuracy of Wave-GAN through its inherent nonlinearities, such response surfaces will be beneficial to conduct fast spectral analyses of wave loads on structures.

Wave-GAN can also bring benefits to the operation stage of offshore and coastal structures. Once a structure is placed, the geographical location's metocean data can be used to calculate the long-term structural dynamics, based on the response surface provided by Wave-GAN. In this way, the rapid deep learning tool may facilitate continuous monitoring of structures in waves, providing the ability to assess structural integrity risks and fatigue, thus improving maintenance and repair strategies over the lifecycle. In addition, a device's response surface built by Wave-GAN could be used to achieve relevant real-time controlling purposes, e.g. controlling the device's dynamics to optimise its performance in the real-time sea condition (Anderlini et al., 2020; Li et al., 2020).

6. Conclusions

This work has developed and presented a novel data-driven computational technique, Wave-GAN based on the Convolutional Neural Networks cGAN principle. It demonstrates the ability to predict three-dimensional nonlinear regular wave loads and run-up on a fixed cylinder by using the Convolutional Neural Networks principle. Datasets used during training and testing of Wave-GAN were constructed using CFD simulations with various wave conditions.

The trained Wave-GAN was subsequently subject to a thorough verification using varied techniques ranging from perceptual observation, MAE evaluation and convergence validation. While minimal deviances in the disturbed wave pattern were observed, this did not impact the prediction of wave profile in other locations. Wave-GAN replicated the CFD results with a high level of accuracy for the wave load, even for the high nonlinearity of the input waves that were close to their breaking point. However, it was observed that the resolution from the predicted images could be increased to potentially allow for easier recognition of the impact loads and improve the average calculated MAE.

Upon verification, the proposed deep learning approach proved the ability to provide comparative results for the prediction of wave load and run-up as obtained using CFD, and Wave-GAN can yield the results in a fraction of time – per the CFD simulation took an average of 6 h to complete whereas Wave-GAN requires only less than 10 s to provide the desired answer. Wave-GAN's rapidity and capability show the potential to be extremely helpful in various design and operation stages.

Finally, despite the extensive usage of Wave-GAN discussed on surrogating CFD, i.e. in a well-trained scope, Wave-GAN can be operated independently from CFD, Wave-GAN is not envisioned to be a complete replacement to CFD or physical experiments, because (a) quality CFD results are always valuable to add training images for the deep learning model, which can continuously expand its applicability and refine its accuracy (b) CFD and experiments are essential to address some extreme operating conditions and very complex structures that are not trained into the deep learning model.

References

Anderlini, E., 2018. Control of wave energy converters using machine learning strategies. University of Edinburgh.

Anderlini, E., Husain, S., Parker, G.G., Abusara, M., Thomas, G., 2020. Towards real-time reinforcement learning control of a wave energy converter. Journal of Marine Science and Engineering 8, 845.

Benites-Munoz, D., Huang, L., Anderlini, E., Marín-Lopez, J.R., Thomas, G., 2020. Hydrodynamic Modelling of An Oscillating Wave Surge Converter Including Power Take-Off. Journal of Marine Science and Engineering 8, 771.

Bre, F., Gimenez, J.M., Fachinotti, V.D., 2018. Prediction of wind pressure coefficients on building surfaces using artificial neural networks. Energy and Buildings 158, 1429–1441.

Brown, S.A., Ransley, E.J., Musiedlak, P.-H., Greaves, D., 2020. Quantifying the predictive capability of OpenFOAM 5.0: Focused wave impacts with floating bodies. International Journal of Offshore and Polar Engineering 30, 20–27.

Buldakov, E., Higuera, P., Stagonas, D., 2019. Numerical models for evolution of extreme wave groups. Applied Ocean Research 89, 128–140.

Chen, L.F., Stagonas, D., Santo, H., Buldakov, E.V., Simons, R.R., Taylor, P.H., Zang, J., 2019. Numerical modelling of interactions of waves and sheared currents with a surface piercing vertical cylinder. Coastal Engineering 145, 65–83.

Cleary, P.W., Rudman, M., 2009. Extreme wave interaction with a floating oil rig: Prediction using SPH. Progress in Computational Fluid Dynamics, an International Journal 9, 332–344.

Dean, R.G., Dalrymple, R.A., 1984. Water wave mechanics for engineers and scientists.

Faltinsen, O.M., Newman, J.N., Vinje, T., 1995. Nonlinear wave loads on a slender vertical cylinder. Journal of Fluid Mechanics 289, 179–198.

Goodfellow, I.J., Pouget-Abadie, J., Mirza, M., Xu, B., Warde-Farley, D., Ozair, S., Courville, A., Bengio, Y., 2014. Generative adversarial networks. arXiv preprint arXiv:1406.2661.

Heins, A.E., 1950. Water waves over a channel of finite depth with a submerged plane barrier. Canadian Journal of Mathematics 2, 210–222.

Huang, L., Ren, K., Li, M., Tuković, Ž., Cardiff, P., Thomas, G., 2019. Fluid-structure interaction of a large ice sheet in waves. Ocean Engineering 182, 102–111.

Huang, L., Tuhkuri, J., Igrec, B., Li, M., Stagonas, D., Toffoli, A., Cardiff, P., Thomas, G., 2020. Ship resistance when operating in floating ice floes: A combined CFD&DEM approach. Marine Structures 74, 102817.

Ioffe, S., Szegedy, C., 2015. Batch normalisation: Accelerating deep network training by reducing internal covariate shift. 32nd International Conference on Machine Learning, ICML 2015 1, 448–456.

Isola, P., Zhu, J.Y., Zhou, T., Efros, A.A., 2017. Image-to-image translation with conditional adversarial networks. Proceedings - 30th IEEE Conference on Computer Vision and Pattern Recognition, CVPR 2017 2017-Janua, 5967–5976. https://doi.org/10.1109/CVPR.2017.632

ITTC, 2017. Uncertainty Analysis in CFD Verification and Validation Methodology and Procedures. Recommended Procedures and Guidelines.

Jacobsen, N.G., Bakker, W., Uijttewaal, W.S., Uittenbogaard, R., 2019. Experimental investigation of the wave-induced motion of and force distribution along a flexible stem. Journal of Fluid Mechanics 880, 1036–1069.

Jiao, J., Chen, C., Ren, H., 2019. A comprehensive study on ship motion and load responses in short-crested irregular waves. International Journal of Naval Architecture and Ocean Engineering 11, 364–379.

Keller, J.B., Karal Jr, F.C., 1960. Surface wave excitation and propagation. Journal of Applied Physics 31, 1039–1046.

Kingma, D.P., Ba, J.L., 2015. Adam: A method for stochastic optimisation. 3rd International Conference on Learning Representations, ICLR 2015 - Conference Track Proceedings.

Krishnakumar, K., 2003. Intelligent systems for aerospace engineering-an overview.

Lee, S., You, D., 2019. Data-driven prediction of unsteady flow over a circular cylinder using deep learning. Journal of Fluid Mechanics 879, 217–254.

Li, C., Wand, M., 2016. Precomputed real-time texture synthesis with markovian generative adversarial networks. Lecture Notes in Computer Science (including subseries Lecture Notes in Artificial Intelligence and Lecture Notes in Bioinformatics) 9907 LNCS, 702–716. https://doi.org/10.1007/978-3-319-46487-9_43

Li, Y., Ong, M.C., Tang, T., 2020. A numerical toolbox for wave-induced seabed response analysis around marine structures in the OpenFOAM® framework. Ocean Engineering 195, 106678.

Li, Y., Ong, M.C., Tang, T., 2018. Numerical analysis of wave-induced poro-elastic seabed response around a hexagonal gravity-based offshore foundation. Coastal Engineering 136, 81–95.

Li, Y.-Y., Park, S., Jiang, J.Z., Lackner, M., Neild, S., Ward, I., 2020. Vibration suppression for monopile and spar-buoy offshore wind turbines using the structure-immittance approach. Wind Energy 23, 1966–1985.

Liu, C., Huang, Z., Tan, S.K., 2009. Nonlinear scattering of non-breaking waves by a submerged horizontal plate: Experiments and simulations. Ocean Engineering 36, 1332–1345.

Liu, S., Gatin, I., Obhrai, C., Ong, M.C., Jasak, H., 2019. CFD simulations of violent breaking wave impacts on a vertical wall using a two-phase compressible solver. Coastal Engineering 154, 103564.

Lyu, S., Huang, L., Thomas, G., 2019. Motions of a Floating Body Induced by Rogue Waves. The 14th OpenFOAM Workshop.

Menter, F., 1993. Zonal two equation kw turbulence models for aerodynamic flows, in: 23rd Fluid Dynamics, Plasmadynamics, and Lasers Conference. p. 2906.

Morison, J.R., Johnson, J.W., Schaaf, S.A., 1950. The force exerted by surface waves on piles. Journal of Petroleum Technology 2, 149–154.

Nichols, C.W., Hirt, B.D., 1979. Volume of Fluid (VOF) Method for the Dynamics of Free Boundaries. Journal of Computational Physics 42, 201–225.

Olaf Ronneberger, Phiipp Fischer, Thomas Brox, 2015. U-Net: Convolutional Networks for Biomedical Image Segmentation. Lecture Notes in Computer Science (including subseries Lecture Notes in Artificial Intelligence and Lecture Notes in Bioinformatics) 9351, 12–20.

O'Mahony, N., Campbell, S., Carvalho, A., Harapanahalli, S., Hernandez, G.V., Krpalkova, L., Riordan, D., Walsh, J., 2019. Deep learning vs. traditional computer vision, in: Science and Information Conference. Springer, pp. 128–144.

Pavlou, D.G., Li, Y., 2018. Seabed Dynamic Response of Offshore Wind Turbine Foundation under Vertical Harmonic Loading: An Analytic Solution. Mathematical Problems in Engineering 2018.

Pena, B., Huang, L., Ahlgren, F., 2020. A Review on Applications of Machine Learning in Shipping Sustainability, in: SNAME Maritime Convention. The Society of Naval Architects and Marine Engineers.

Peña, B., McDougall, A., 2016. An Investigation Into the Limitations of the Panel Method and the Gap Effect for a Fixed and a Floating Structure Subject to Waves, in: International Conference on Offshore Mechanics and Arctic Engineering. American Society of Mechanical Engineers, p. V007T06A048.

Pena, B., Muk-Pavic, E., Thomas, G., Fitzsimmons, P., 2019. Numerical analysis of a leading edge tubercle hydrofoil in turbulent regime. Journal of Fluid Mechanics 878, 292–305.

Rabault, J., Ren, F., Zhang, W., Tang, H., Xu, H., 2020. Deep reinforcement learning in fluid mechanics: A promising method for both active flow control and shape optimisation. Journal of Hydrodynamics 32, 234–246.

Rainey, R.C.T., 1989. A new equation for calculating wave loads on offshore structures. Journal of Fluid Mechanics 204, 295–324.

Rajendran, S., Fonseca, N., Soares, C.G., 2016. Prediction of extreme motions and vertical bending moments on a cruise ship and comparison with experimental data. Ocean Engineering 127, 368–386.

Reich, Y., 1997. Machine learning techniques for civil engineering problems. Computer-Aided Civil and Infrastructure Engineering 12, 295–310.

Rrake, E., Pena, B., Moschonas, K., 2015. An Investigation into the Motion Behaviour of a Wind Farm Mothership, in: SNAME WMTC.

Viquerat, J., Rabault, J., Kuhnle, A., Ghraieb, H., Larcher, A., Hachem, E., 2021. Direct shape optimisation through deep reinforcement learning. Journal of Computational Physics 428, 110080.

Windt, C., Davidson, J., Ransley, E.J., Greaves, D., Jakobsen, M., Kramer, M., Ringwood, J.V., 2020. Validation of a CFD-based numerical wave tank model for the power production assessment of the wavestar ocean wave energy converter. Renewable Energy 146, 2499–2516.

Young, T., Hazarika, D., Poria, S., Cambria, E., 2018. Recent trends in deep learning based natural language processing. ieee Computational intelligenCe magazine 13, 55–75.

Zhao, H. jun, Song, Z. yao, Li, L., Kong, J., Wang, L. qiang, Yang, J., 2016. On the fifth-order Stokes solution for steady water waves. China Ocean Engineering 30, 794–810. https://doi.org/10.1007/s13344-016-0051-5